THE AMERICAN MINERALOGIST, VOL. 54, NOVEMBER–DECEMBER, 1969

SLIP SYSTEMS IN QUARTZ: I. EXPERIMENTS

R. D. BAËTA[1] AND K. H. G. ASHBEE,
H. H. Wills Physics Laboratory, University of Bristol, England.

ABSTRACT

Single crystals of synthetic quartz were cut into compression test specimens of various orientations and deformed at elevated temperatures and at atmospheric pressure. No macroscopic evidence of plastic flow was detected at an imposed strain rate of 10^{-3} sec.$^{-1}$. At an imposed strain rate of 10^{-4} sec^{-1}, plastic flow was possible only at temperatures above 600°C and, with a strain rate of 10^{-5} sec^{-1}, there was plastic flow at 575°C and above. Below 700°C slip, was predominantly basal and in a crystallographic ***a*** direction. Between 700°C and 850°C, slip occurred with equal facility in the crystallographic ***a*** and ***c*** directions, and on many low index planes co-zonal with these directions. At 750°C and above, slip also occurred on pyramidal planes and in the directions $<a+c>$. These observations are discussed in terms of the nature of dislocation cores in quartz.

INTRODUCTION

In an earlier paper (Baëta and Ashbee, 1967), evidence was reported for the plastic deformation at atmospheric pressure of synthetic crystals of quartz at temperatures close to or within the high-quartz field. The present work concerns a systematic investigation of this deformation in order to identify all the slip systems which can be operated at atmospheric pressure. Since the elastic strain energy of a dislocation is proportional to the modulus of its Burgers vector squared (Frank and Nicolas 1953), dislocations with small Burgers vectors are favoured. Thus, for high-quartz, the most likely Burgers vectors are ***a*** $<\bar{1}\bar{1}20>$ and ***c*** [0001], of lengths 5.02 Å and 5.48 Å respectively. In the present investigations, single crystal specimens were compressed in each of six orientations in order to subject different low index planes containing the vectors ***a***, ***c*** or $<a+c>$ to the highest resolved shear stress. The observed slip systems are reported, and structural considerations which would influence the choice of slip vectors are discussed.

In part II of this work, linear anisotropic elasticity theory is used to estimate the non-core energies of dislocations in quartz, and the "ease of slip" for several dislocations is considered. In particular, the criterion for basal and/or prismatic slip is discussed. Details of the stress-stain behaviour in the compressed specimens, and the effects of crystal phase changes on the mode of deformation, are to be published elsewhere.

EXPERIMENTAL

Compression test specimens were cut in the form of rectangular parallelopipeds from synthetic quartz crystals grown by the General Electric Company, Wembley. The dimen-

[1] Present address: Department of Physics, University of Ghana, Legon, Ghana.

sional details of these specimens are given in Table 1, and the compression axes for the six orientations used, designated as $\perp a, \perp A, \perp B, \perp c, \perp z$ and $\perp m$ respectively, are shown in Figure 1. The surfaces of each specimen were polished to mirror smooth finish using increasingly finer grades of carborundum paper, and subsequently, on cloths impregnated with diamonds of 6 μm, 1 μm and finally $\frac{1}{4}$ μm particle size. Parallelism of opposite surfaces was achieved by using a polishing device which incorporates a steel guard ring.

All tests were carried out with a type-E "Hounsfield" tensometer incorporating a compression jig and a small "Kanthal" wound furnace which fits concentrically over "Sintox" compression p'attens. This is a "hard-beam," constant cross-head speed machine with an AC load cell. Before testing, each specimen was examined optically with ordinary and

TABLE 1. DIMENSIONAL DETAILS OF THE COMPRESSION SPECIMENS

Compression axis (length 6.75 mm)	Broad face (width 2.75 mm)	Narrow face (width 2.00 mm)
$\perp B$(45° to [0001])	near $(11\bar{2}2)$	$(1\bar{1}00)$
$\perp a$(parallel to $[\bar{1}\bar{1}20]$)	(0001)	$(1\bar{1}00)$
$\perp m$(parallel to $[1\bar{1}00]$)	$(11\bar{2}0)$	(0001)
$\perp Z$(90° to $[\bar{1}011]$)	$(1\bar{2}10)$	near $(20\bar{2}3)$
$\perp A$(70° to [0001])	$(1\bar{1}00)$	near $(11\bar{2}6)$
$\perp C$(parallel to [0001])	$(1\bar{1}00)$	$(11\bar{2}0)$

polarized light microscopes to check for the absence of macroscopic internal defects. The incidence of cracking during low⇌high phase transformations was avoided by using a programmed heating cycle in which the heating or cooling rate near the transformation temperature was 2°C per minute.

After deformation, each specimen was examined with both polarizing and phase contrast microscopes using reflected and transmitted light. A scanning electron microscope was also used in order to resolve minute topographic detail on some specimens. Stereographic projections were used to determine the slip systems from the orientations of slip steps and of stress birefringence bands.

DETERMINATION OF SLIP SYSTEMS

Compression axis $\perp B$ *(45° to both* **c** *[0001] and* **a** *$[\bar{1}\bar{1}20]$*) Figure 2 shows an optical transmission micrograph taken with crossed polars, through the $(1\bar{1}00)$ face of a specimen compressed at 900°C. The strong stress birefringence bands running N.W.–S.E. are parallel to the (0001) plane. Below 900°C, equally well developed interesecting bands occur due to slip on the (0001) and $(11\bar{2}0)$ planes as shown in Figure 4(c). In most tests, slip lines were observed on the near $(11\bar{2}2)$ faces only, and were parallel to the trace of the compressed surfaces, Figure 4(b). Consequently, the active slip systems must be (0001) $[\bar{1}\bar{1}20]$ and $(11\bar{2}0)$ [0001].

Specimens plastically deformed by more than 3 percent in the temperature range 700°–850°C, showed evidence of slip on the additional systems $(10\bar{1}0)$ [0001], $(01\bar{1}0)$ [0001], and a weakly developed $(1\bar{1}03)$ $[\bar{1}\bar{1}20]$. An interesting feature of the mode of deformation is that it di-

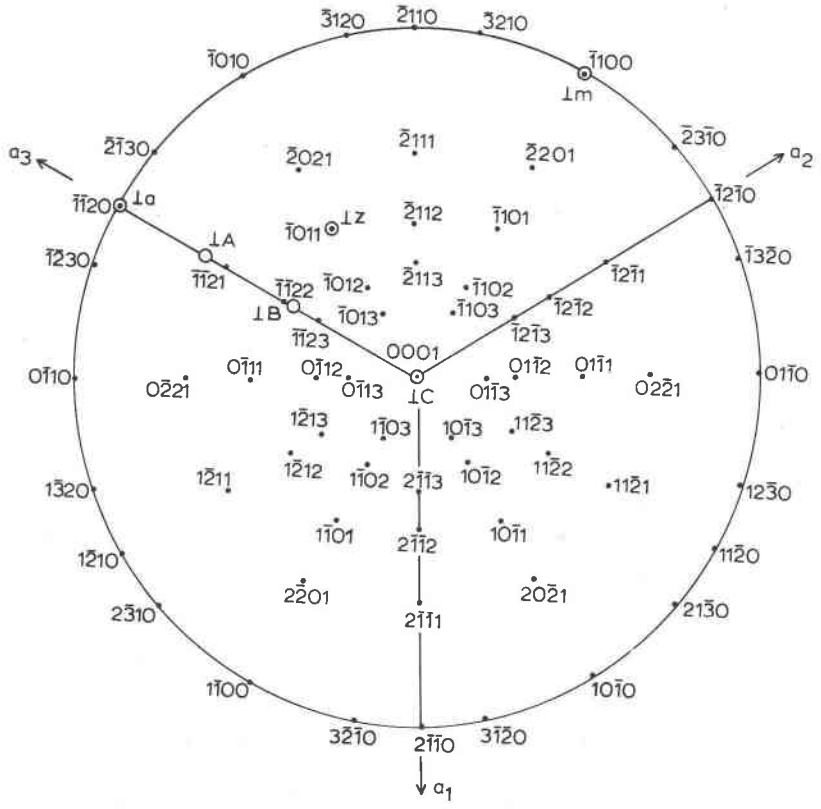

FIG. 1. Standard stereographic projection of (0001) plane of quartz, showing the six orientations (indicated by circles) of compression.

vides the crystal into blocks, each block having slipped on different systems (Baëta and Ashbee 1967).

In tests performed at temperatures above 850°C, slip is mainly basal (cf. Fig. 2), as in the case of tests performed below 700°C. Similar changes in the mode of deformation with increasing test temperature were observed in specimens compressed in other orientations, and are believed to be related to changes in crystal structure.

Compression axes ⊥a and ⊥m (parallel to [$\bar{1}\bar{1}20$] and to [$1\bar{1}00$]. These are described together because symmetry considerations necessitate identical resolved shear stresses on the low index planes of high-quartz compressed in these two orientations.

Figure 3 shows a specimen plastically compressed ⊥*a* by 2.1 percent at

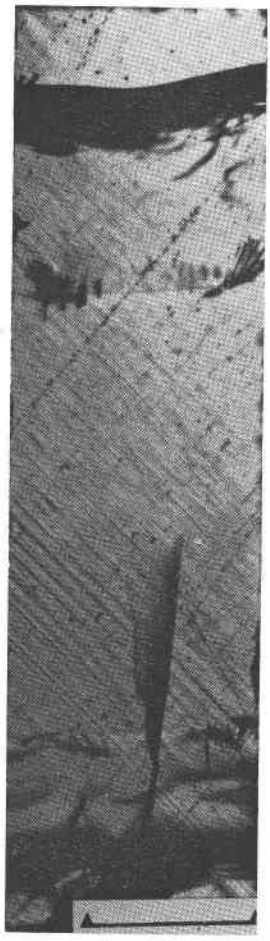

FIG. 2. Stress birefringence pattern after 3% plastic strain at a strain rate of 10^{-5} sec^{-1} at 900°C. Compression axis 45° to [0001], microscope axis perpendicular to $(1\bar{1}00)$. (Bar scale = 1.0 mm).

FIG. 3. Optical transmission micrograph (polarized light) after 2.1% plastic compression along $[\bar{1}\bar{1}20]$ at a strain rate of 10^{-5} sec^{-1} at 800°C. Microscope axis normal to (0001). (Bar scale = 1.0 mm).

800°C. This micrograph was recorded with transmitted polarized light normally incident through the (0001) face. Intersecting birefringence bands due to slip can be seen in the transparent regions of the crystal. The broad areas of extinction, especially down the middle of the crystal, are due to cracks. Narrow, vertically oriented "lesions" are also evident.

Specimens compressed $\perp a$, had slip lines only on the $(1\bar{1}00)$ faces, and

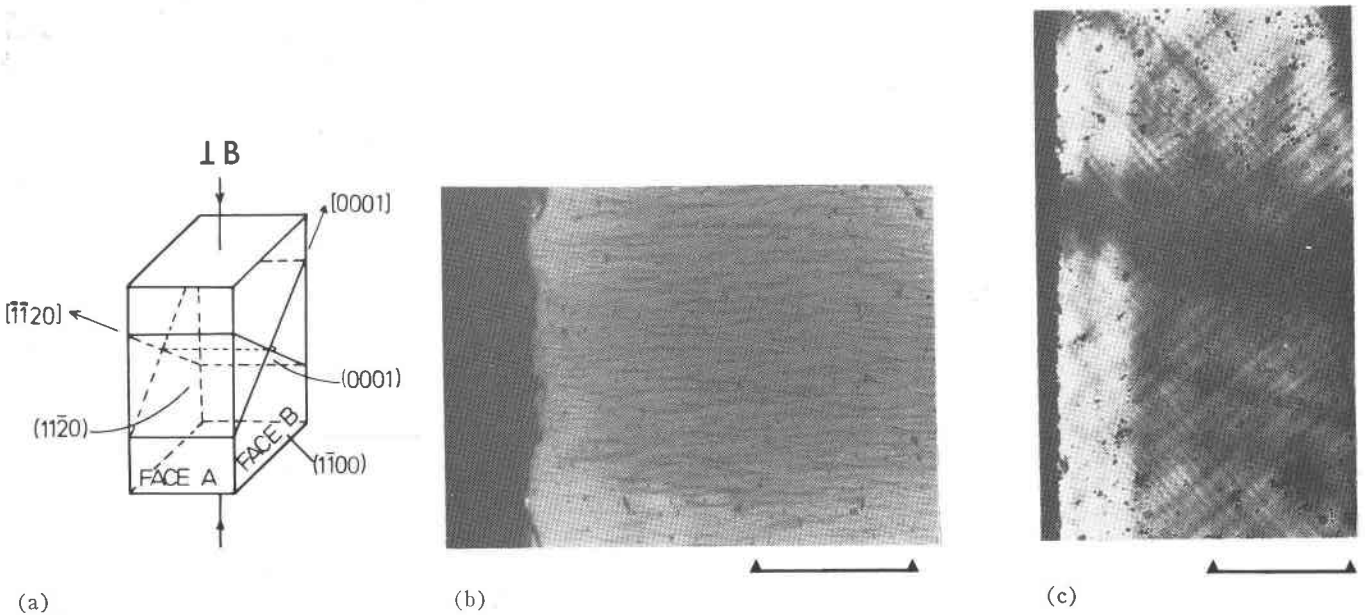

FIG. 4. (a) Orientation of $\perp B$ test specimen. (b) Slip lines on the near (11$\bar{2}$2) face, after 2% plastic strain at a strain rate of 10^{-5} sec^{-1} at 800°C. (Bar scale = 0.1 mm) (c) Stress-birefringence pattern through the (1$\bar{1}$00) face of the same specimen. (Bar scale = 0.2 mm).

these were oriented parallel to the trace of the compressed surfaces, Figure 5(b). Birefringence bands were observed only through the (0001) face, Figures 3 and 5(c), and correspond to slip on $(10\bar{1}0)$ and $(01\bar{1}0)$ planes. Since there were no slip lines on the (0001) faces, the slip directions evidently lie in the (0001) plane, and the slip systems must be $(10\bar{1}0)$ $[\bar{1}2\bar{1}0]$ and $(0\bar{1}\bar{1}0)$ $[2\bar{1}\bar{1}0]$.

In the high-quartz temperature range, specimens compressed $\perp m$ yielded at the same stresses as specimens compressed $\perp a$. The orientations of the birefringence bands (seen only through the (0001) face) and of slip steps (seen only on the $(11\bar{2}0)$ faces) showed that the same $(10\bar{1}0)$ $[\bar{1}2\bar{1}0]$ and $(01\bar{1}0)$ $[2\bar{1}\bar{1}0]$ slip systems were active.

The modes of deformation change at temperatures above 900°C. Although slip still occurs on the same planes, the appearance of differently oriented slip steps indicates the incidence of new slip directions. For example, Figure 6 shows slip steps, as well as vertical cracks, produced on a (0001) face of a crystal deformed $\perp a$ at 1000°C. Since there should be no resolved shear stress parallel to **c** [0001], it is concluded that the new slip systems are $(10\bar{1}0)$ $[\bar{1}2\bar{1}3]$ and $(01\bar{1}0)$ $[2\bar{1}\bar{1}3]$. Similar evidence has been obtained for slip on the same systems at temperatures above 900°C, in specimens compressed $\perp m$.

An interesting feature observable in Figure 6 (also in Fig. 14), is the patchy areas of white contrast concentrated at the intersections of glide bands. These are evidence for local recrystallization into a phase of silica different from quartz, the details of which are to be published elsewhere.

Compression axis $\perp z$ (*perpendicular to z* $(\bar{1}011)$). Figure 7 shows a specimen viewed between crossed polars through the $(1\bar{2}10)$ face after 3.1 percent plastic compression at 800°C. Figure 9(*b*) and (*c*) show the appearances of slip steps observed on the near $(20\bar{2}3)$ and $(1\bar{2}10)$ faces respectively. Stereographic analysis of the orientations of the birefringence bands (Fig. 7) and of the slip steps reveals that the active slip planes are $(\bar{1}010)$, $(0\bar{1}12)$, $(\bar{1}102)$, $(\bar{1}013)$, (0001), $(11\bar{2}0)$ and $(2\bar{1}\bar{1}0)$. The presence of slip steps on all faces of the specimen precludes absolute identification of the slip directions. However, it should be noted that each of the above planes contains either or both of the directions $\boldsymbol{a}\langle\bar{1}\bar{1}20\rangle$ or **c**[0001].

Compression axis $\perp A$ (*70° to* **c** [*0001*]) This orientation of compression axis was chosen in order to achieve a higher resolved shear stress on the *r* $(0\bar{1}11)$ plane and in an $\boldsymbol{a} <\bar{1}\bar{1}20>$ direction, than on the *c* (0001) and *m* $(10\bar{1}0)$ planes in an $\boldsymbol{a} <\bar{1}\bar{1}20>$ direction. However, all three types of slip systems appeared to be active even during the smallest measurable

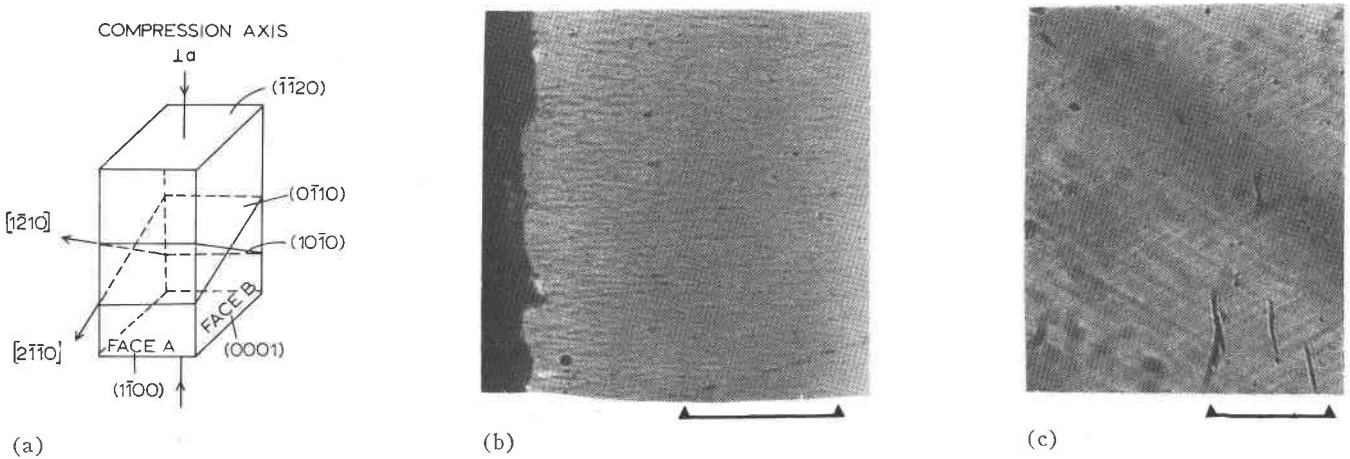

FIG. 5. (a) Orientation of $\perp a$ test specimen. (b) Slip lines on the $(1\bar{1}00)$ face of specimen compressed parallel to $[\bar{1}\bar{1}20]$ by 2% at a strain rate of 10^{-6} sec^{-1} at 800°C. (c) Birefringence bands seen through the (0001) face of the same specimen. (Bar scales = 0.1 mm).

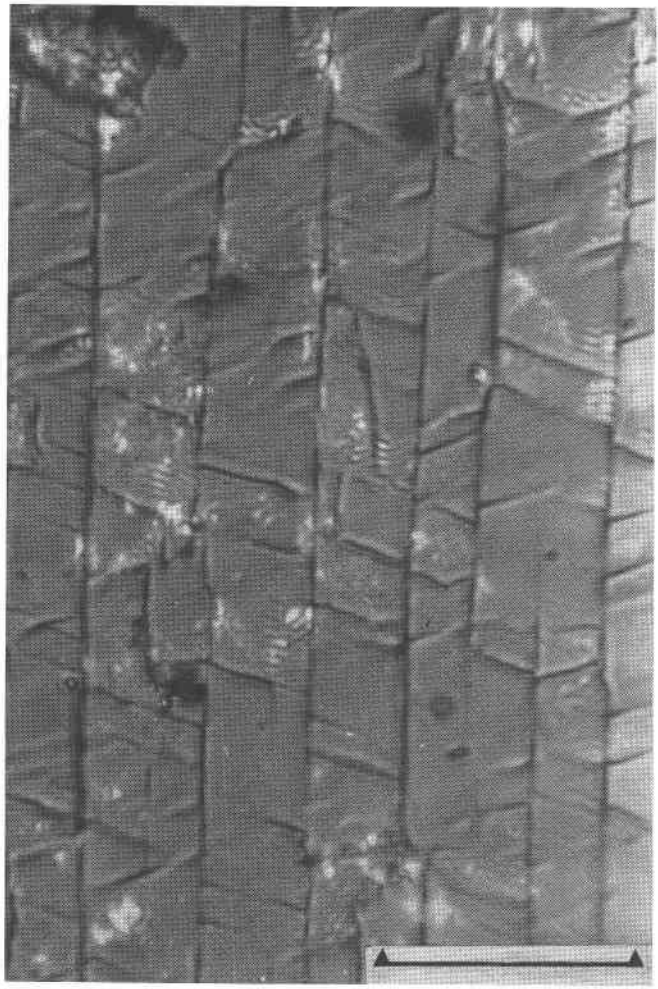

FIG. 6. Surface markings on the (0001) face of a specimen compressed parallel to [$\bar{1}\bar{1}$20] by 2% at a strain rate of 10^{-5} sec^{-1} at 1000°C. (Bar scale = 0.1 mm).

plastic strain. Figure 8 shows an optical transmission micrograph of a specimen viewed between crossed polars after 2 percent plastic deformation at 800°C. In addition to stress birefringence, contrast due to kinking and to fracture can be seen. Analysis of the orientations of birefringence bands and slip steps shows that the active glide planes are ($\bar{1}$011), ($\bar{1}$010), (0$\bar{1}$11), (0$\bar{1}$10), (0$\bar{1}$12), ($\bar{1}$012), (0001) and, for plastic strains of 3.5 percent, ($\bar{1}$013). It is assumed that the respective slip directions are parallel to ***a*** <$\bar{1}\bar{1}$20> directions.

FIG. 7. Stress birefringence bands produced by 3.1% plastic compression perpendicular to $(\bar{1}011)$ at a strain rate of 10^{-5} sec^{-1} at 800°C. Microscope axis perpendicular to $(1\bar{2}10)$. (Bar scale = 1.0 mm).

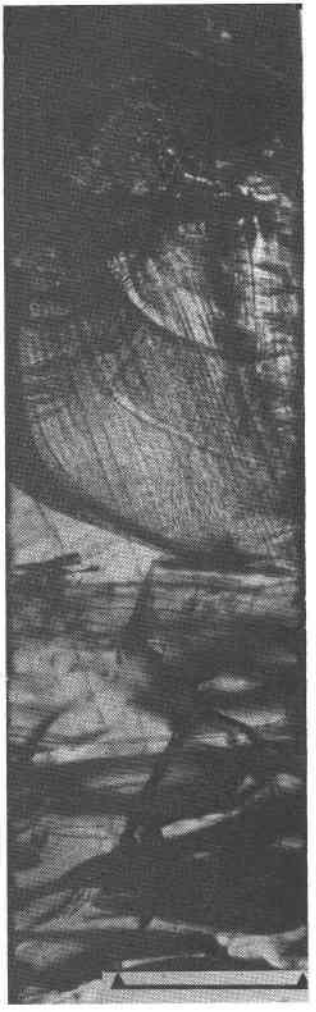

FIG. 8. Transmission optical micrograph of a specimen viewed between crossed polars and through $(1\bar{1}00)$, after 2% plastic compression in a direction 70° from [0001] towards $[\bar{1}\bar{1}20]$. Strain rate 10^{-5} sec^{-1}, temperature 800°C. (Bar scale = 1.0 mm).

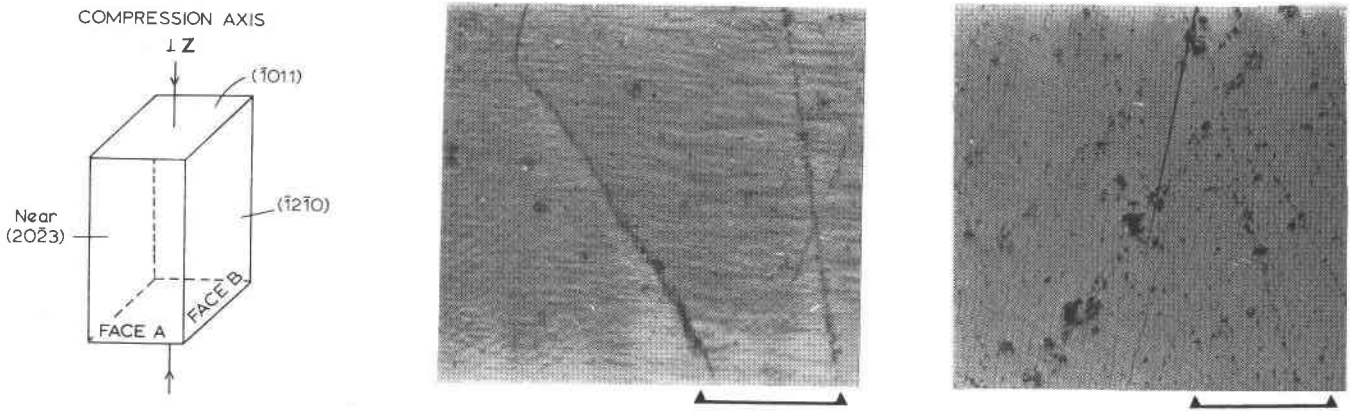

FIG. 9. (a) Orientation of the $\perp z$ test specimen. (b) and (c) Surface markings on the near (20$\bar{2}$3) and (1$\bar{2}$10) faces respectively of a specimen compressed by 1% at a strain rate of 10^{-5}sec^{-1} at 800°C. (Bar scales = 0.1 mm).

Compression axis $\perp c$ (*parallel to* **c** [*0001*]). Tests with this direction of compression were carried out in order to investigate the possibility of slip in directions inclined to both basal and prismatic planes. As was the case for other orientations, the deformation behaviour above 850°C was different from that observed within the high-quartz temperature range.

Figures 10(a) and (b) show optical transmission micrographs taken through the $(1\bar{1}00)$ and $(11\bar{2}0)$ faces respectively of a specimen viewed

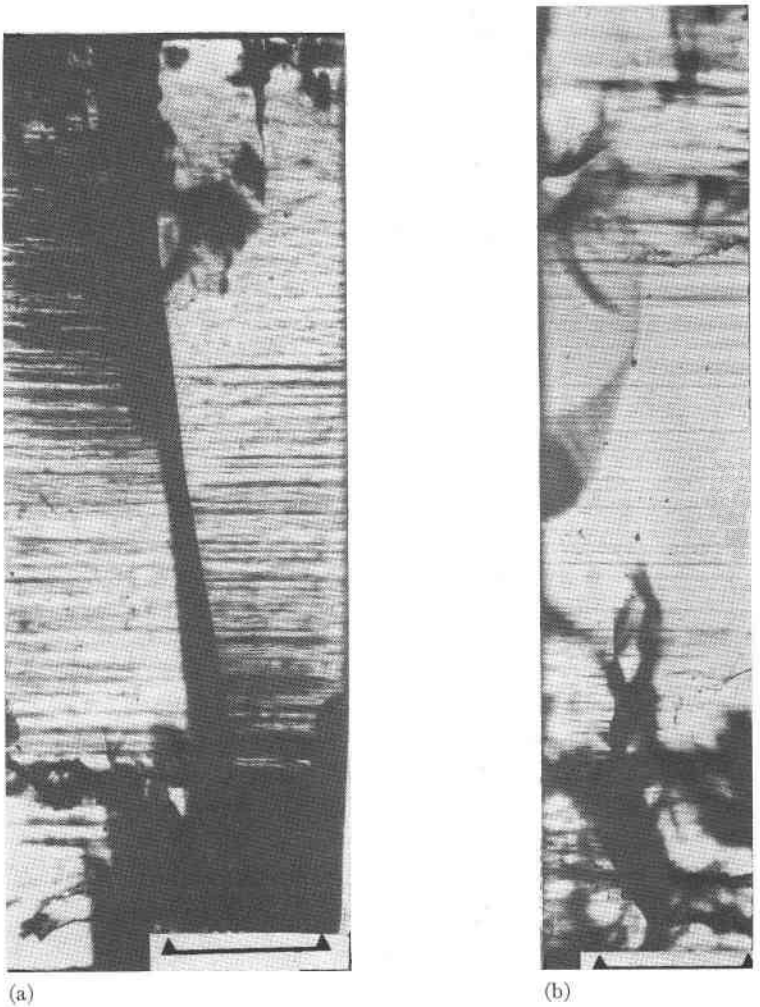

(a) (b)

FIG. 10. Optical transmission micrographs (crossed polars) of a specimen compressed along [0001] by 2.1% at a strain rate of 10^{-5} sec^{-1} at 800°C. (a) through the $(1\bar{1}00)$ face, and (b) through the $(11\bar{2}0)$ face. (Bar scales = 1.0 mm).

between crossed polars after 2.1 percent compression at 800°C. The birefringence bands are evidently parallel to c (0001), the plane of compression. Examination at higher magnification, Figure 11(b) and (c), reveals the presence of birefringence bands inclined to the basal plane. Deformation also produces surface markings parallel to c (0001) and these are best resolved by the scanning electron microscope, especially after lightly etching with hydrofluoric acid. A typical micrograph is shown in Figure 12. The slip planes deduced from all these observations are $(11\bar{2}2)$, $(1\bar{1}22)$, $(1\bar{1}01)$ and $(\bar{1}101)$. Possible slip directions for each of these planes are $<\bar{1}\bar{1}23>$.

It is evident in Figure 12, that both faces are marked with streaky lines parallel to the compression axis. At higher magnification, Figures 13(a) and (b), these streaks are clearly resolved as short, vertical "lesions."

The deformation modes at temperatures beyond the high-quartz range are remarkably different. Figures 14(a) and (b) show the appearance of slip steps on $(11\bar{2}0)$ and $(1\bar{1}00)$ faces respectively after compression at 950°C. Plastic deformation appears to have occurred in blocks having boundaries parallel to low index planes. Stereographic analysis of the slip line orientations within these blocks shows that slip has taken place on $\{11\bar{2}1\}$, $\{11\bar{2}2\}$, $\{10\bar{1}1\}$, $\{10\bar{1}3\}$ and possibly on $\{11\bar{2}3\}$. Possible slip directions for the first three planes are $<\bar{1}\bar{1}23>$, and for the last two planes, are $<\bar{2}111>$.

Another mode of very high temperature deformation is illustrated in Figure 15(a). The specimen has become divided into basal slabs which are alternately plastically deformed and undeformed. The lateral spread in the deformed regions has been achieved by slip on the intersecting systems revealed by the fine slip steps. Figure 15(b) shows the same face after lightly etching with hydrofluoric acid. It is evident that there is a very high density of dislocations in the "hills", whereas the "valleys", representing the undeformed slabs, appear to be almost dislocation free. During compression, the plastic slabs create a lateral drag and therefore tension in the adjacent rigid slabs. Eventually, this creates longitudinal cracks in the latter as can be seen in Figure 16.

A summary of the slip directions and slip planes identified by the present observations, is given in Table 2. Confirmative evidence of the Burgers vectors of slip dislocations, obtained from thin film transmission electron microscopy has been reported elsewhere (Baëta and Ashbee 1968).

Dislocation Cores

The slip directions positively identified in the present work are parallel

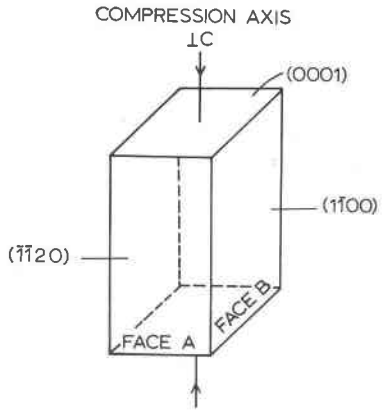

(a)

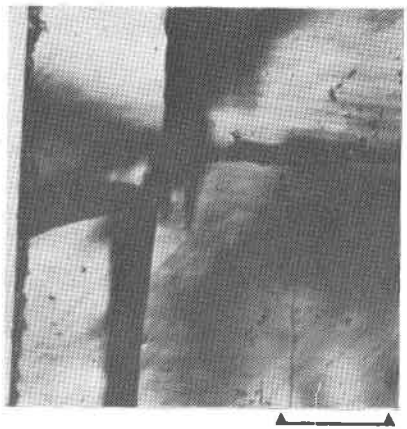

(b)

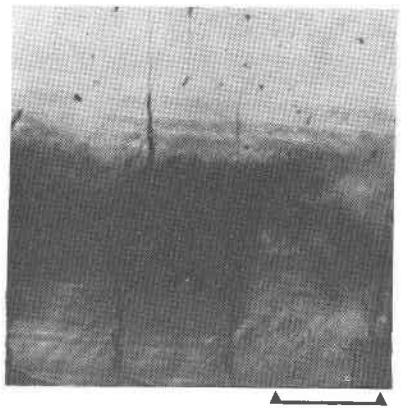

(c)

FIG. 11. (a) Orientation of $\perp C$ test specimen. (b), (c), Higher magnification micrographs of Figures 10(a) and (b) respectively. (Bar scales = 0.1 mm).

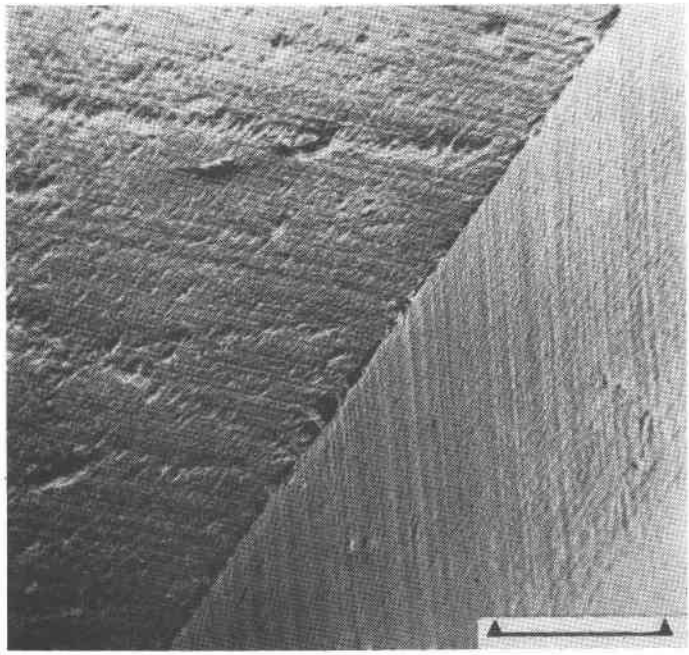

FIG. 12. Scanning electron micrograph showing adjacent faces of a specimen compressed parallel to [0001] by 2% at a strain rate of 10^{-5} sec^{-1} at 800°C. Specimen etched for 10 min. in concentrated HF. (Bar scale = 0.1 mm).

to the lattice vectors $\boldsymbol{a}$, $\boldsymbol{c}$ and $<\boldsymbol{a}+\boldsymbol{c}>$. The same slip directions in quartz deformed under hydrostatic pressure have been reported previously by Christie and Green (1964), and by Griggs and Blacic (1965). The follow-

TABLE 2. SLIP DIRECTIONS AND SLIP PLANES IN HIGH-QUARTZ

Slip direction	$\lvert b \rvert$ Å	Slip plane	d Å
1) $\langle 11\bar{2}0 \rangle$	5.02	(0001)	5.48
		$\{1\bar{1}00\}$	4.44
		$\{1\bar{1}01\}$	3.41
		$\{1\bar{1}02\}$	2.32
		$\{1\bar{1}03\}$	1.68
2) [0001]	5.48	$\{1\bar{1}00\}$	4.44
		$\{11\bar{2}0\}$	2.51
3) $\langle 11\bar{2}3 \rangle$	7.44	$\{1\bar{1}01\}$	3.41
		$\{11\bar{2}1\}$	2.28
		$\{11\bar{2}2\}$	1.85

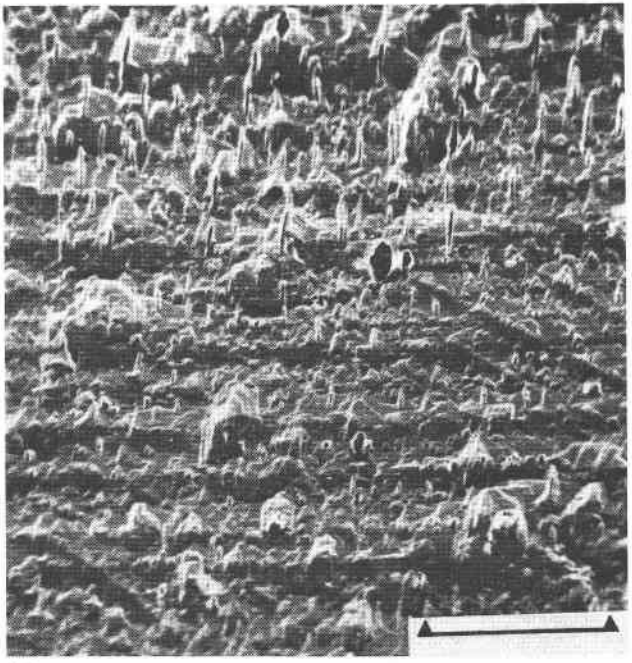

(a)

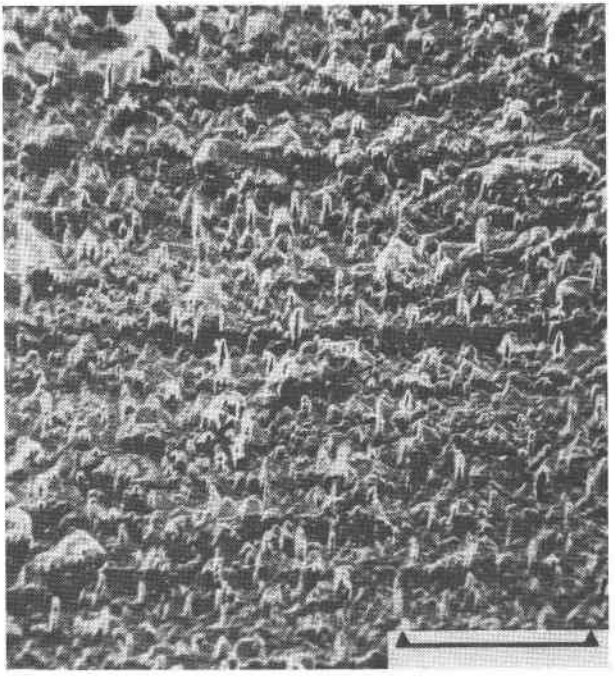

(b)

FIG. 13. (a), (b). High magnification scanning electron micrographs of the two faces shown in Figure 12. (Bar scale=0.05 mm).

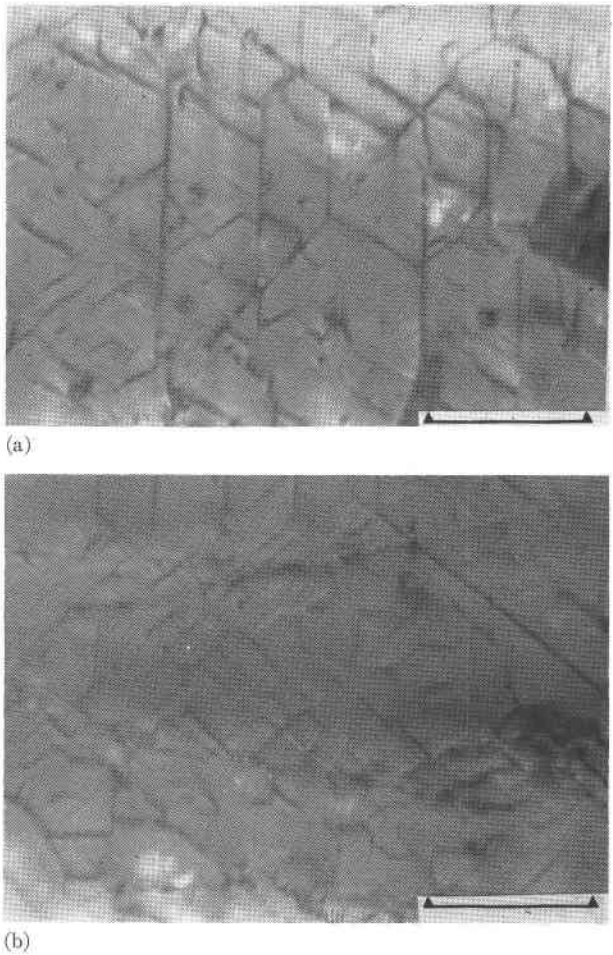

(a)

(b)

FIG. 14. Slip steps on the (a) $(11\bar{2}0)$ and (b) $(1\bar{1}00)$ faces of a specimen compressed parallel to [0001] by 2% at a strain rate of 10^{-5} sec^{-1} at 950°C. (Bar scale=0.1 mm).

ing discussion draws attention to an interesting structural characteristic of the cores of dislocations whose Burgers vectors are $\boldsymbol{a}$, $\boldsymbol{c}$, or $<\boldsymbol{a}+\boldsymbol{c}>$.

The basic structural unit of all forms of silica is the "SiO_4" tetrahedron-in which a silicon atom fits interstitially between four oxygen atoms. This unit is extremely stable, and it is only the stacking and distortion of this unit which varies from one form of silica to another. Consequently, the presence and motion of dislocations might also be expected to be such that the SiO_4 tetrahedral unit itself is maintained more or less intact.

Although the following discussion refers to the high-quartz structure, the situation is maintained during the high→low transition; the SiO_4

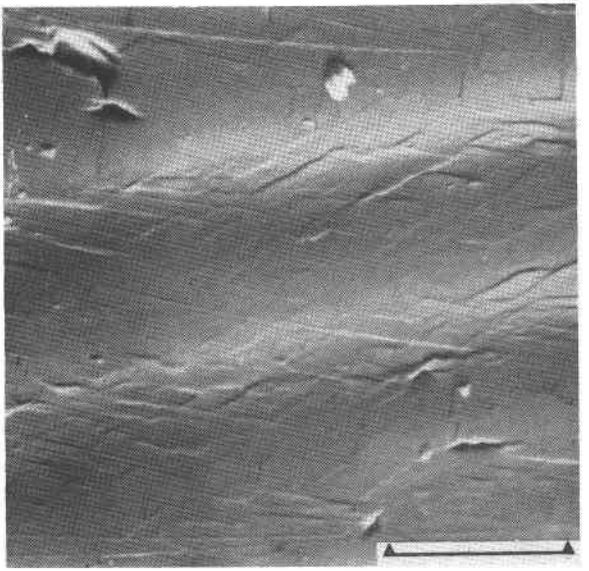

(a)

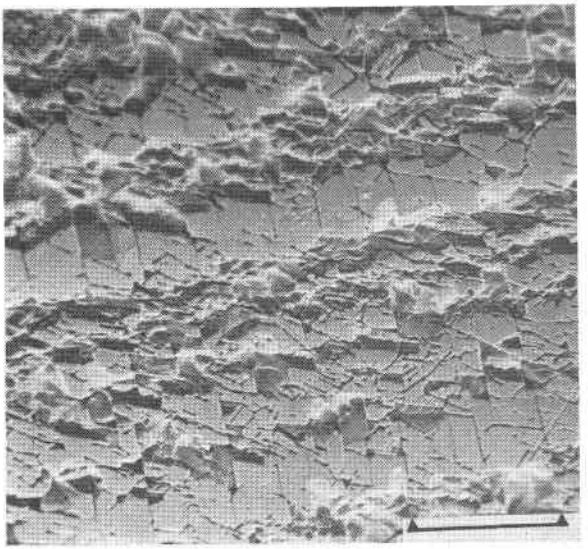

(b)

FIG. 15. Scanning electron micrographs of a $(11\bar{2}0)$ face of a specimen compressed parallel to [0001] by 2% at a strain rate of 10^{-5} sec^{-1} at 900°C. (a) before etching (Bar scale=0.01 mm), (b) after etching for 10 min. in concentrated HF. (Bar scale=0.02 mm).

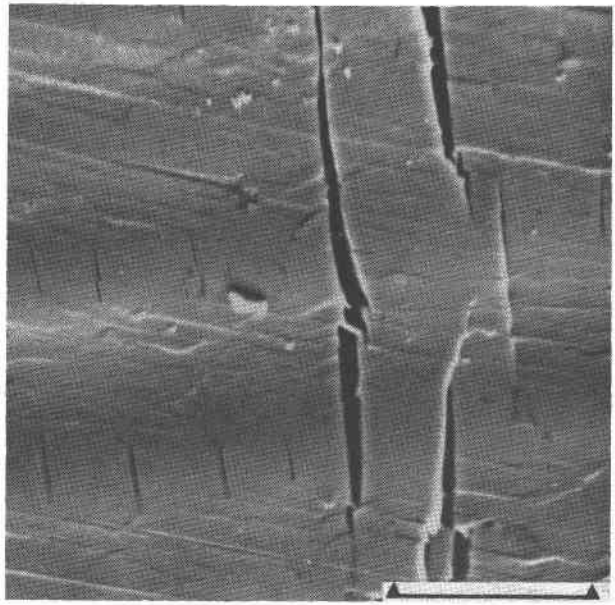

FIG. 16. Scanning electron micrograph showing longitudinal cracks in alternate basal slabs of a specimen compressed parallel to [0001]. (Bar scale=0.01 mm).

tetrahedra are merely slightly rotated away from the high-quartz positions in such a way as to destroy one set of two-fold axes.

Dislocations with Burgers vector $\boldsymbol{a}$. In the perfect high-quartz structure there are two kinds of channel parallel to each lattice vector $\boldsymbol{a}$. Both channels are defined by helices of SiO_4 tetrahedra, whose body centred silicon atoms lie along the edges of prisms, the cross-sections of which are a parallelogram for one channel, and an irregular hexagon for the other.

The two kinds of channel can be clearly seen in Figure 17(a), which shows the structure of right-handed ($P6_222$) high-quartz projected on to the $(1\bar{1}20)$ plane. The full circles in the figure represent the positions of the silicon atoms, and the open circles represent the oxygen atoms. The limits of the unit cell in the projection are represented by the broken lines. The numbers on the line joining the silicon atoms A, A' are the fractional heights (in the units of "c") above the (0001) plane of silicon atom A. The other numbers in the projection denote the heights of the atoms above the projection plane, with 20 units corresponding to $|\boldsymbol{a}|$.

Figure 17(b) shows an SiO_4 tetrahedra model of part of the quartz structure, viewed along the channel whose cross-section is a parallelogram. This channel will subsequently be referred to as the rhombic channel.

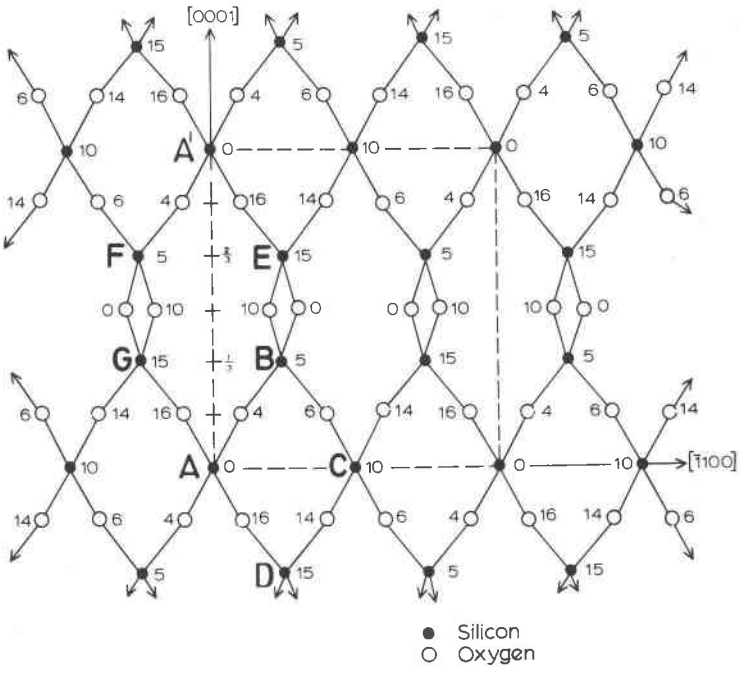

(a)

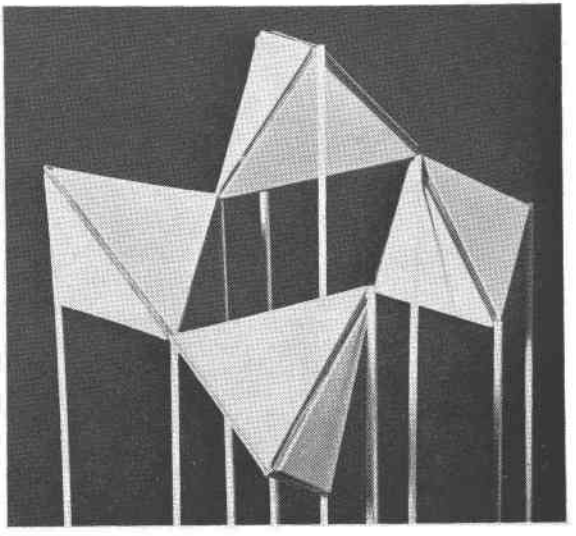

(b)

FIG. 17. High-quartz structure viewed along an a-axis. (a) Projection on $(\bar{1}\bar{1}20)$, (b) SiO_4 tetrahedra model showing the "rhombohedral" channel; each tetrahedron has oxygen atoms at its corners, and a silicon atom at its center.

It is evident in Figure 17 that the rhombic channel represented by the silicon atoms *ABCDA* is defined by a helix of SiO_4 tetrahedra, with four tetrahedra per pitch, the pitch being equal in magnitude to the Burgers vector $|\boldsymbol{a}|$. The hexagonal channel, *ABEA'FGA* is defined by a helix of six SiO_4 tetrahedra, with pitch equal to twice the modulus of the Burgers vector. It should be noted that the two helices are of opposite sense; thus in structurally right-handed (morphologically left-handed) quartz, the hexagonal helix is right-handed while the rhombic helix is left-handed, and vice versa in structurally left-handed (morphologically right-handed) quartz.

If a screw dislocation is introduced along the axis of the rhombic channel, the helix changes either into rings of four SiO_4 tetrahedra or into a helix with double pitch, depending on the sign of the Burgers vector. On the other hand, a screw dislocation along the axis of the hexagonal channel changes the pitch of this helix to either one half or three halves, again depending on the sign of the Burgers vector. For either channel, it is evidently unlikely that dislocations of opposite sign will have the same line tensions. Since SiO_4 tetrahedra are known to form stable rings in silicates (Zoltai and Buerger 1960), it could be intuitively argued that dislocations whose cores create a smaller rather than a larger pitch are favoured. Furthermore, since the two helices are of opposite sense, the favoured Burgers vectors in the two channels will be of opposite sign.

It is evident from Figure 17(a) that adjacent hexagonal channels share a common side. Hence for slip in the basal plane, it is possible for screw dislocations to move through hexagonal channels only, resulting in slip on planes which are very nearly atomically flat. However, a dislocation along the axis of a rhombic channel has to pass through a hexagonal channel in order to reach the next rhombic channel and, for basal slip, this necessitates a corrugated slip plane. For a rhombohedral plane $\boldsymbol{r}$, however, slip via both kinds of channel defines a fairly smooth surface since adjacent hexagonal and rhombic channels share a common side, see Figure 17(a).

There is another important structural feature associated with the glide of screw dislocations with Burgers vector $\boldsymbol{a}$. The effect of a screw dislocation along the axis of either channel is to compress or extend its helix, depending on the sign of the Burgers vector. Both deformations will disdistort and rotate the individual tetrahedra in a helix, causing displacements perpendicular to the Burgers vector. A screw dislocation moving through the hexagonal channels only either compresses or extends the helices, depending on the sign of the Burgers vector. On the other hand, since the helices in the two kinds of channel are of opposite sense, a screw dislocation gliding via both kinds alternately compresses one helix and

extends the next. This latter mode can, of course, be avoided in the case of basal slip involving the hexagonal channels only.

Finally, it should be noted that the atomic displacements produced by the presence of an edge dislocation are essentially the same as those produced by a screw dislocation. For example, the Burgers vector which creates a tube of four-member rings of SiO_4 tetrahedra along a screw dislocation, creates a thin sheet of the same rings along the edge segment of the same dislocation. However, the distortions and rotations of individual SiO_4 tetrahedra at the core of an edge dislocation will be different from those at a screw dislocation core.

Dislocations with Burgers vector ***c***. The discussion presented above also applies to a screw dislocation with Burgers vector ***c***. Figure 18 shows the

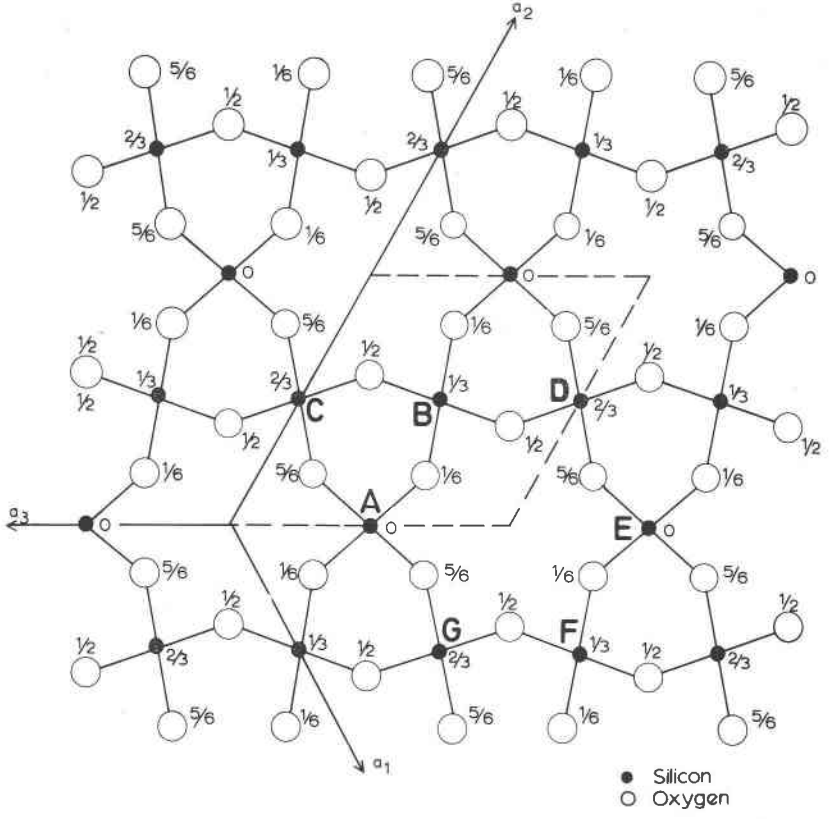

FIG. 18. Projection of high-quartz structure on (0001).

structure of right-handed high-quartz ($P6_222$) projected on to the (0001) plane. The unit cell is indicated by the broken lines; the full circles represent silicon atoms and the open circles oxygen atoms. In this case, the cross-sections of the channels defined by the SiO_4 helices are respectively a regular triangle such as $ABCA$, and a regular hexagon such as $ABDEFGA$.

There are three tetrahedra per pitch on the triangular helix, and the pitch is equal in magnitude to the Burgers vector $|\boldsymbol{c}|$. The hexagonal helix has six tetrahedra per pitch, the pitch being equal to twice the modulus of the Burgers vector. The two helices are again of opposite sense, but in this case, it is the triangular helix that has the same sense as the structural hand, while the hexagonal helix has the opposite sense. (The situation is reversed in morphological terminology).

If a screw dislocation is placed along the axis of the triangular channel, the helix changes either into three-member rings of SiO_4 tetrahedra or into a helix with double pitch, depending on the sign of the Burgers vector. Similarly, a screw dislocation along the axis of the hexagonal channel changes the pitch of the helix to either one half, or three halves, again depending on the sign of the Burgers vector.

Similar arguments apply to the motions of a screw dislocation with Burgers vector $\boldsymbol{c}$, as were deployed in the foregoing section for the motions of a screw dislocation with Burgers vector $\boldsymbol{a}$.

Dislocations with apparent Burgers vector $<\boldsymbol{a}+\boldsymbol{c}>$. The nature of the dislocations responsible for glide in $<\bar{2}113>$ directions is not clear. For example, transmission electron microscopy has not revealed dissociation of dislocations with Burgers vector $<\boldsymbol{a}+\boldsymbol{c}>$ into pairs of dislocations with Burgers vectors $\boldsymbol{a}$ and $\boldsymbol{c}$ respectively. On the other hand, if dissociation occurs, then there is no reason why both of the resultant dislocations should multiply and glide at the same rates, thereby producing net cooperative shear parallel to $<\boldsymbol{a}+\boldsymbol{c}>$. Whatever the answer to this dilemma, it is evident that as far as dislocation cores are concerned, the net distortion can be resolved into its components, i.e. into the core structures discussed above.

The force on a dislocation in quartz. Because of the characteristic structures of dislocation cores in quartz, it is of interest to inquire into the nature of the force acting on a dislocation line when an external stress is applied to the crystal.

The Peach-Koehler (1950) equation for the force acting on a dislocation can be written as

$$dF = (b_j \cdot \sigma_i) \times dl$$

where σ_{ij} is the stress tensor in the crystal (excluding the self-stress of the dislocation), and each element dl of the dislocation is acted upon by the force dF tending to produce atomic displacements parallel to the Burgers vector b_j. As far as the long range elastic stress field is concerned, a screw dislocation for example, can be regarded as a straight line. However, at the core of the dislocation, the question arises as to whether the dislocation line is to be regarded as a helix. The mean dl is parallel to the axis of the helix, and hence for a homogeneously applied stress field, it would not matter whether the dislocation is regarded as a helix or as a straight line. However, in an inhomogeneously applied stress field, such as is produced in a compression test due to the end constraints on the test specimen, or such as the elastic field due to nearby dislocations, there may be a difference in regarding the dislocation as a line or as a helix. The local stress is expected to vary from one element of dl to the next in the helix, resulting in non-uniform displacements of segments of the dislocation line. This would evidently resist the dislocation's motion through the lattice.

Another consequence of the nature of dislocations in quartz arises from the difference in the core distortions for dislocations with Burgers vectors $\pm \boldsymbol{b}$. This is because in the one case, the helix is extended, and in the other case compressed, resulting in the different core energies mentioned earlier. Thus dislocations of one sign may be preferred, in which case the operation of Frank-Read sources, for example, is expected to be restricted.

ACKNOWLEDGMENT

One of us (R.D.B.) was supported by the University of Ghana.

REFERENCES

BAËTA, R. D. AND K. H. G. ASHBEE (1967) Plastic deformation of quartz at atmospheric pressure. *Phil. Mag.* **15,** 931–938.

———, AND ——— (1968) Evidence of plastic deformation of quartz at atmospheric pressure. *4th Eur. Regional Conf. Electron Microscopy. Rome,* p. 427.

CHRISTIE, J. M., AND H. W. GREEN (1964) Several new slip mechanisms in quartz. *Trans. Amer. Geophys. Union* **45,** 103.

FRANK, F. C., AND J. F. NICOLAS (1953) Stable dislocations in the common crystal lattices. *Phil. Mag.* **44,** 1213–1235.

GRIGGS, D. T., AND J. D. BLACIC (1965) Quartz: Anomalous weakness of synthetic crystals. *Science* **147,** 292–295.

Manuscript received, April 14, 1969; accepted for publication, July 29, 1969.